JAST, Vol. 13, No 2, pp 53-60

JAST
Journal of Aerospace Science and Technology

Science Article

Two-Phase CFD Modeling of Three-Dimensional Supercavitating Flows

Ali Cheraqi[1]*, Reza Ebrahimi[2]
1-2 Combustion and Propulsion Research Laboratory, Faculty of Aerospace Engineering, K.N.Toosi University of Technology
* Tehran, Daneshgah Boulevard, Ehsan Street Exit
Email: *Cheraqi@email.kntu.ac.ir

One of the most effective ways of high-speed motion in water is the motion in the supercavitation regime. This way provides the possibility to avoid considerable viscose resistance of boundary layer and consequently reach to very small drag coefficient which can be several times smaller than, that of the continuous flow. In this study the numerical simulation of developed and supercavitating flow is performed. The CFX code which served as a platform for the present work is a three-dimensional code that solves the Reynolds-Averaged Navier-Stokes equations with a finite volume method. The cavitation model is implemented based on the use of Rayleigh-Plesset equation to estimate the rate of vapor production. A high Reynolds number form κ-ε model is implemented to provide turbulence closure. For steady state flows and poor mesh resolution near the wall (using log-law wall functions), there is a priori no difference between the two equations formulations. For the different case studies, multi-block structured meshes were generated and the numerical simulation is performed in a wide range of cavitation numbers. Results are presented for steady state flows with natural cavitation about various bodies. Comparisons are made with available measurement of surface pressure distribution, cavitation bubble geometry (cavity length and cavity width) and drag coefficient. The simulated results are in a good agreement with the experimental data. Finally, the three-dimensional results are presented for a submerged body running at several angles of attack.

Keywords: *Two-Phase Flow, Homogeneous Model, Supercavitation, Mass-Transfer*

Introduction

Supercavitation is a phenomenon in which a cavity is formed behind the underwater vehicle, when it travels at very high speeds. In order to generate a cavity that encloses the entire body, the vehicle should have a high thrust force to maintain such high speeds to counteract the effect of drag force. Usually, the drag can be characterized as hydrodynamic drag and viscous drag. In the case of supercavitation, the hydrodynamic drag is considerably much higher than the viscous drag, since the body does not come into contact with the fluid. Therefore, the viscous drag is ignored in this phenomenon. The hydrodynamic drag can be obtained using the integral of the pressure distribution, caused by the fluid flow, at the nose of body. In the current study the numerical simulation is performed for steady state cavitation flows about disk and cone cavitator with and without after-body.

The tendency for a flow to cavitate is characterized by the cavitation number, defined as:

$$\sigma = \frac{p - p_v}{0.5\rho U^2} \qquad (1)$$

1 PhD student (Correspondence Author)
2 Professor

Received: 21 Feb. 2020
Accepted: 08/ March 2020

where p is a reference pressure for the flow, p_v is the vapor pressure for the liquid, and the denominator represents the dynamic pressure. Clearly, the tendency for a flow to cavitate increases as the cavitation number is decreased. With reduce of the cavitation number, five different regimes are observed in the cavitated flow including: incipient- , sheet- , partial- , and super-cavitation.

Catvitation is treated separately from thermal phase change, as the cavitation process is typically too rapid for the assumption of thermal equilibrium, at interface to be correct. In the simplest cavitation models, mass transfer is driven by purely mechanical effects, namely liquid-vapor pressure differences, rather than thermal effects.

Computational modeling of cavitation has been pursued for years. Early studies primarily utilize the potential flow theory; they are still widely used in many engineering applications. Studies dealing with cavitation modeling through the computation of the Navier-Stokes equations have emerged in the last decade. Recently, to account for the cavitation dynamics in a more flexible manner, the multiphase transport equation-based models (TEM) are developed. A review of these studies is presented here; Singhal et al. [1], Merkle et al. [2], Kunz et al. [3], [4] and [5], Suaer and Schnerr [6] and Senocak et al. [7] and [8] have employed similar models based on this concept with differences in the source terms. One apparent advantage of this model comes from the convective character of the equation, which allows modeling of the impact of the inertial forces on cavities like elongation, detachment and drift of bubbles. Merkle et al. [2] and Kunz et al. [3], [4] and [5] have employed the artificial compressibility method. Also, Kunz et al. have adopted a non-conservative form of the continuity equation and applied the model to different geometries.

In the current research, the multiphase mixture model is used, and the Rayleigh-Plesset model is implemented in the multiphase framework as an inter-phase mass transfer model.

GOVERNING EQUATION

The set of governing equations include of the conservative form of the Reynolds-Averaged Navier-Stokes equations for the homogeneous mixture multiphase flows, with an additional volume fraction transport equation to account for the inter-phase mass transfer, denoted in the Cartesian coordinates, as follow [9]:

$$\frac{\partial \rho_m}{\partial t} + \vec{\nabla} \cdot (\rho_m \vec{U}_m) = 0 \tag{2}$$

$$\frac{\partial}{\partial t}(\rho_m \vec{U}_m) + \rho_m (\vec{U}_m \cdot \vec{\nabla}) \vec{U}_m = -\vec{\nabla}(p_m) + \vec{\nabla} \cdot (\bar{\bar{\tau}} + \bar{\bar{\tau}}_t) + \vec{M}_m + \vec{f} \tag{3}$$

$$\frac{\partial (\alpha_l \rho_l)}{\partial t} + \vec{\nabla} \cdot (\alpha_l \rho_l \vec{U}_m) = \Gamma_l = \dot{m}_l^v + \dot{m}_l^c \tag{4}$$

where α_l represent the liquid phase volume fraction. The mixture density and the turbulent viscosity respectively are defined as [9]:

$$\rho_m = \sum_{n=1}^{2} \alpha_n \rho_n \tag{5}$$

$$\mu_m = \sum_{n=1}^{2} \alpha_n \mu_n \tag{6}$$

the density of each constituent is considered to be constant. The mass transfer rates from vapor to liquid and from liquid to vapor are denoted $\dot{m}^v$ and $\dot{m}^c$, respectively.

Mass Transfer

The Rayleigh-Plesset equation provides the basis for the rate equation controlling vapor generation and condensation. The Rayleigh-Plesset equation describing the growth of a gas bubble in liquid is given by:

$$R_B \frac{dR_B}{dt} + \frac{3}{2}\left(\frac{dR_B}{dt}\right)^2 + \frac{2\sigma'}{R_B} = \frac{p_v - p}{\rho_l} \tag{7}$$

where R_B represents the bubble diameter, p_v is the pressure in the bubble that is assumed to be the vapor pressure at the liquid temperature, p is the pressure in the liquid surrounding the bubble and σ' is the surface tension coefficient between the liquid and vapor. Note that this is derived from a mechanical balance, assuming no thermal barriers to bubble growth. By neglecting the second order terms and the surface tension, this equation reduces to:

$$\frac{dR_B}{dt} = \sqrt{\frac{2}{3}\left(\frac{p_v - p}{\rho_l}\right)} \tag{8}$$

The total inter-phase mass transfer rate per unit volume is:

$$\dot{m} = N_B \frac{dm_B}{dt} = \frac{3\alpha_v \rho_v}{R_B} \sqrt{\frac{2}{3}\left(\frac{|p_v - p|}{\rho_l}\right)} \tag{9}$$

This expression has been derived assuming bubble growth (vaporization). It can be generalized to include condensation as follows [9]:

$$\dot{m}_l^c = F\frac{3\alpha_v\rho_v}{R_B}\sqrt{\frac{2}{3}(\frac{|p_v-p|}{\rho_l})}\,\mathrm{sgn}(p_v-p) \quad (10)$$

where F is an empirical factor which may differ for condensation and vaporization, designed to account for the fact that they may occur at different rates (condensation is usually much slower than vaporization).

Despite the fact that Eq. (9) has been generalized for vaporization and condensation, it requires further modification in the case of vaporization. Vaporization is initiated at nucleation sites (most commonly non-condensable gases). As the vapor volume fraction increases, the nucleation site density must decrease accordingly, since there is less liquid. For vaporization, α_v in Eq. (10) is replaced by $\alpha_{nuc}(1-\alpha_v)$ to give [9]:

$$\dot{m}_l^v = -F\frac{3\alpha_{nuc}(1-\alpha_v)\rho_v}{R_B}\sqrt{\frac{2}{3}(\frac{|p_v-p|}{\rho_l})}\,\mathrm{sgn}(p_v-p) \quad (11)$$

α_{nuc} is a volume fraction of the nucleation sites Eq. (11), is maintained in the case of condensation. Note that in this model R_B represents the diameter of the nucleation sites. To obtain an inter-phase mass transfer rate, further assumptions regarding the bubble concentration and radius are required [9].

Turbulence Model and Wall Function

In this work a standard form $k-\varepsilon$ model with wall functions is implemented to provide turbulence closure. For homogeneous multiphase flow, bulk turbulence equations are solved which are the same as the single-phase equation, except that the mixture density and the mixture viscosity are used. As with velocity, the turbulence scalars are illustrated as being mixture quantities ([9] and [10]):

$$\frac{\partial(\rho k)}{\partial t}+\vec{\nabla}\cdot(\rho\vec{U}k)=\vec{\nabla}\cdot\left[(\mu+\frac{\mu_t}{\sigma_k})\vec{\nabla}k\right]+P_k-\rho\varepsilon \quad (12)$$

$$\frac{\partial(\rho\varepsilon)}{\partial t}+\vec{\nabla}\cdot(\rho\vec{U}\varepsilon)=\vec{\nabla}\cdot\left[(\mu+\frac{\mu_t}{\sigma_\varepsilon})\vec{\nabla}\varepsilon\right]+\frac{\varepsilon}{k}(C_{\varepsilon1}P_k-C_{\varepsilon2}\rho\varepsilon) \quad (13)$$

where $C_{\varepsilon1}$, $C_{\varepsilon2}$, σ_K and σ_ε are constants and p_k is the turbulence production due to the viscous forces in Eq. (13), which is modeled using [9]:

$$P_k=\mu_t\vec{\nabla}\vec{U}\cdot(\vec{\nabla}\vec{U}+\vec{\nabla}U^T)-\frac{2}{3}\vec{\nabla}\cdot\vec{U}(3\mu_t\vec{\nabla}\cdot\vec{U}+\rho k)+P_{kb} \quad (14)$$

In the present work, the wall function approach is an extension of the method of Launder and Spalding ([10]). In the log-law region, the near wall tangential velocity is related to the wall shear stress by means of a logarithmic relation. The formulation of the standard wall functions has the problem of the singularity at the separation points where the near wall velocity vanishes. The problem of inconsistencies in the wall function in the case of fine meshes can be overcome with the use of the special wall function formulation here. It can be applied on arbitrarily fine meshes and allows you to perform a consistent mesh refinement independent of the Reynolds number of the application [9].

NUMERICAL SOLUTIONS

Solver

The CFX commercial code, which is served as a platform for the present work is a three-dimensional unstructured mesh code that solves the Reynolds-Averaged Navier-Stokes equations with a finite volume method. The solver is fully coupled and solves the hydrodynamic equations (*u, v, w, p*) in a single system. This solution approach uses a fully implicit discretization of the equations at any given time step. For the steady state problems, the time-step behaves like an acceleration parameter, to guide the approximate solutions in a physically based manner to a steady-state solution. The solver uses a multi-grid accelerated Incomplete Lower Upper (ILU) factorization technique for solving the discrete system of linearized equations. An algebraic Multigrid technique is used carrying out early iterations on a fine mesh, and later iterations on progressively coarser virtual ones. The results are then transferred back from the coarsest mesh to the original fine mesh. The reader can refer to CFX solver theory [9] and to specific techniques in computational fluid dynamics for more details.

Advection Scheme

The discretization of the advection terms is as follow [9]:

$$\phi=\phi_{up}+\beta\nabla\phi\cdot\Delta\vec{r} \quad (15)$$

where ϕ_{up} is the value at the upwind node, $\vec{r}$ is the vector from the upwind node to the computed node, and $\beta\nabla\phi\cdot\Delta\vec{r}$ is called numerical advection correction and is as an anti-diffusive flux added to the upwind scheme. $\beta=0$ leads to the first order upwind difference scheme, and $\beta=1$ is formally second order accurate. The high-resolution scheme that is used in the current study, locally computes β to be as close to 1 as possible (reducing to first order near discontinuities and in the free stream where the solution has little variation) [9].

Boundary Conditions

Velocity components, water and vapor volume fraction, turbulence intensity, and length scale are specified at inlet boundaries and extrapolated at outlet boundaries. Pressure distribution is specified at outlet boundaries (the parameter which fixes the cavitation number) and extrapolated at inlet boundaries. At walls, velocity components and turbulence quantities are enforced using wall functions, pressure and volume fractions are extrapolated.

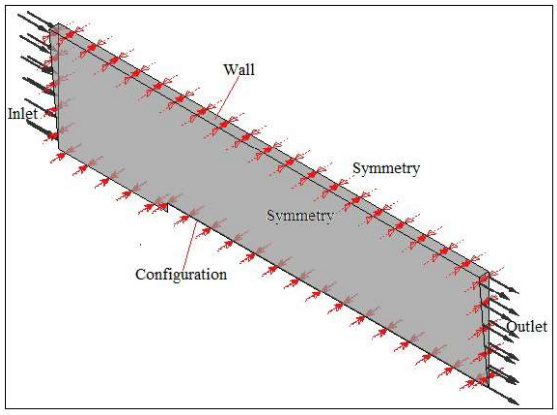

Fig 1: The computational domain and imposed boundary conditions for a blunt fore-body.

Mesh Study

In order to properly assess grid resolution requirements, a range of grid sizes is used. In Fig 2, liquid volume fraction contours, selected streamlines and the grid are illustrated for selected cavitation number. For the blunt configuration, 200x40, 280x60 and 350x70 mesh cells are run. Fig 3 demonstrates that differences between predicted surface pressures for the medium and fine meshes are small, with increase of mesh cells to 420x80 there is no different between distributions of pressure coefficient. Note that s arc length along configuration and d maximum diameter of body. The fine meshes are used for all subsequent calculations presented current research. For fine-grid near wall points are established at locations yielding $10<y+<100$ (Fig 4).

Summary of mesh influence for different case study is listed in table 1.

Table 1: mesh influence for different case study

Configuration	Mesh cells
disk	200x50+150x10, 280x60+200x20, 350x70+250x30, 420x80+300x40
cone	240x40+150x10, 340x60+250x30, 440x80+300x40
Blunt body	200x40, 280x60, 350x70, 420x80
Cone with after body	240x40, 340x60, 440x80

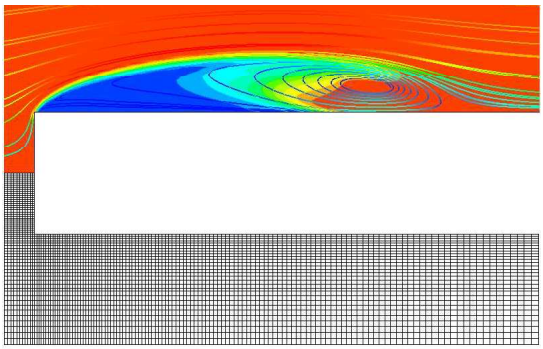

Fig 2: Predicted liquid volume fraction, selected streamlines and computational grid for a blunt fore-body at $\sigma=0.3$.

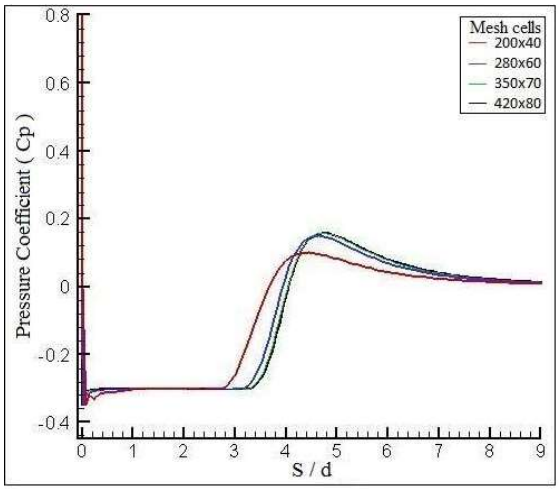

Fig 3: comparison of predicted surface pressure distribution

for a blunt fore-body at $\sigma = 0.3$.

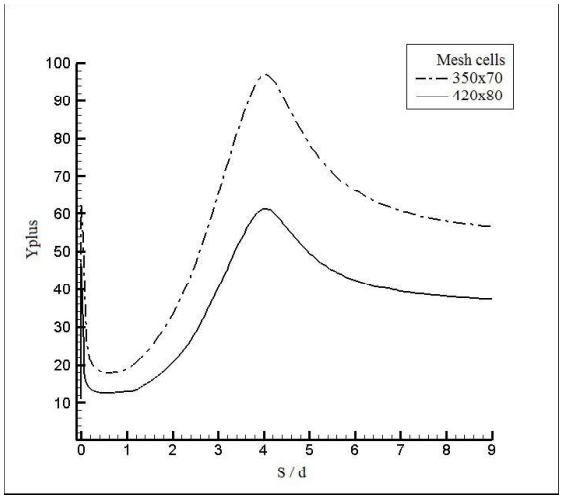

Fig 4: Yplus profile for a blunt fore-body at $\sigma = 0.3$.

RESULTS AND DISSCUTIONS

Axisymmetric Results

Two sets of results by the authors are presented here. The first set includes axisymmetric steady-state analyses of natural cavitation about several configurations. These solutions are compared to semi-empirical and experimental measurements to demonstrate the capability of the employed model. The second set of results includes a variety of three-dimensional analysis of supercavitating flows of relevance to high-speed vehicles. In order to demonstrate the three-dimensional capability of the method, a model of the blunt fore-body configuration is studied follow is run at numerous angles of attack.

In this section results are presented for steady state cavitation flows about disk and cone cavitator. The pressure distribution on the wetted surface of disk for $\sigma = 0.24$ is showed in Fig 5a. There is close agreement with experimental measurement of Rouse and McNown [11]. The corresponding Reynolds number is 284569 based on maximum cavitator diameter (d=1.27cm).

Drag coefficient for disk cavitator presented in Fig 5b, exhibit a total variation in $C_D/1+\sigma$ of under 1 percent clearly demonstrating the accuracy of Reichardt's semi-empirical formula, which treats it as constant.

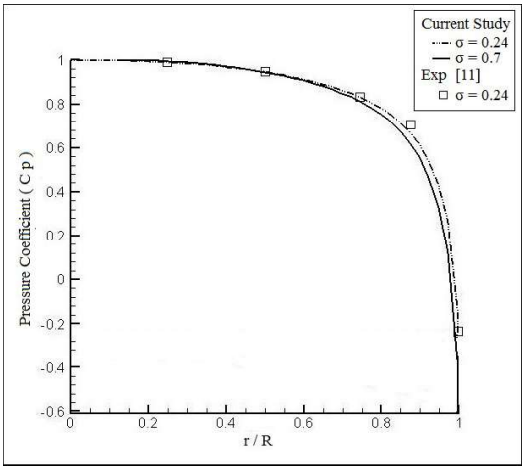

(a)

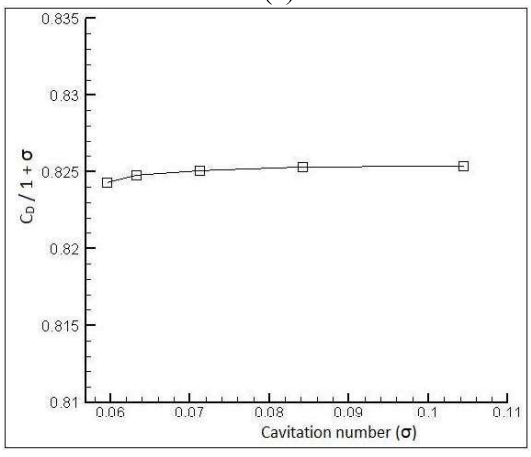

(b)

Fig 5: distribution of pressure coefficient on the wetted surface of the disk (a), variation of drag coefficient for infinity of length of cavity (b)

Cavitation bubble geometry (cavity length and cavity width) and drag coefficient are the main characteristics of axisymmetric supercavitation. In Reichardt work in a horizontal free-jet water tunnel he found the cavities to be ellipsoids with axes given by the semi-empirical expression [13].

$$\frac{L}{d_{\max}} = \frac{\sigma + 0.008}{\sigma(1.7\sigma + 0.066)} \qquad (16)$$

He also found the relation between drag and cavity width to be [13]:

$$\frac{d_{\max}}{d} = \left[\frac{C_D(\sigma)}{\sigma(1 - 0.132\sigma^{1/2})}\right]^{1/2} \qquad (17)$$

where L, $d_{max,}$ and d, are cavity length, maximum diameter of the cavity and the diameter of the cavitator respectively. Reichardt suggested $C_D(0)$ for disks to be 0.80 and relation for $C_D(\sigma)$ as follow [13]:

$$C_D(\sigma) = C_D(0)[1 + \sigma] \qquad (18)$$

In Figs 6 liquid volume fraction contours are illustrated for the disk and the cone cavitators with specified cavitation numbers.

The main parameter of the cavity ($L/d, D_{\max}/d$) are compared with the experimental measurement of Self and Ripken [12], and with Reichardt semi-empirical formula in Fig 7. Reichardt experiments were limited to $\sigma \le 0.12$, and the Eq. (18) is arbitrarily extrapolated to higher cavitation numbers in these figures.

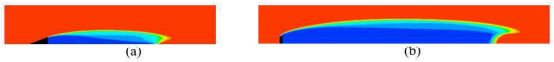

Fig 6: liquid volume fraction contours for conical (a) and blunt (b) fore-body without after-body at $\sigma = 0.15$.

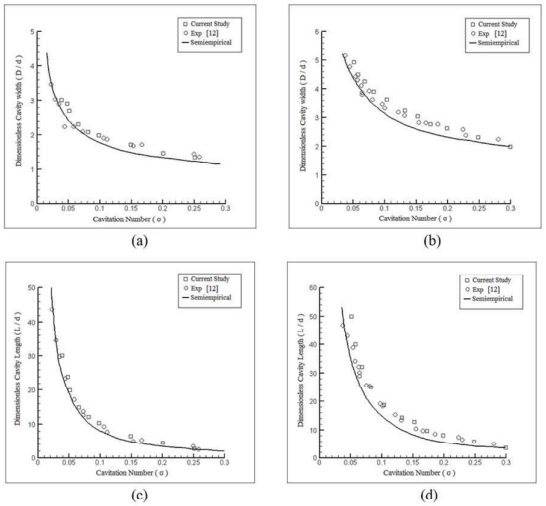

Fig 7: supercavity parameter (D/d and L/d) vs. cavitation number for a cone (a, c) and disk (b, d) cavitator.

Furthermore, in the current study, two configurations of the Rouse-McNown [11] experimental work are also analyzed. These included 0-caliber (blunt), and conical (45° cone angle) cavitator shapes with cylindrical after-body. The corresponding Reynolds number based on maximum cavitator diameter (d=2.54cm) is 136000.

In Figs 8a and 8b field liquid volume fraction contours are illustrated for selected cavitation numbers.

Figs 9a and 9b show comparisons between predicted and measured surface pressure distributions for conical and blunt configurations at specified cavitation number. In this figures s is arc length along configuration and d is diameter of body. The achieved results are in good agreement with those of experimental measurements.

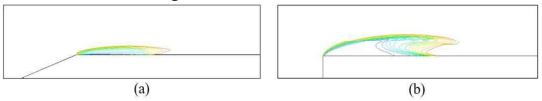

Fig 8: liquid volume fraction contours for conical (a) and blunt (b) fore-body with after-body at $\sigma = 0.3$.

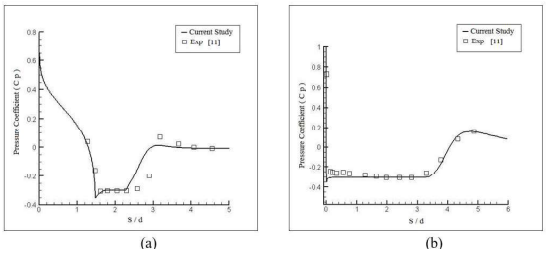

Fig 9: comparison of numerical and experimental surface pressure distribution at $\sigma = 0.3$ for conical (a) and blunt (b) fore-body.

Three Dimensional Results:

In Fig 10 are showed sample results of a three-dimensional simulation of cavitating flow over a blunt body for angles of attack of 0°, 2.5°, 5°, 7.5° and 10°. These plots include sample streamlines and the cavitation bubble shape as identified with an isosurface of $\alpha_l = 0.8$. A 420x80x80 mesh corresponding to the fine mesh size previously mentioned in grid studies is generated. The corresponding cavitation number in these figures is 0.29.

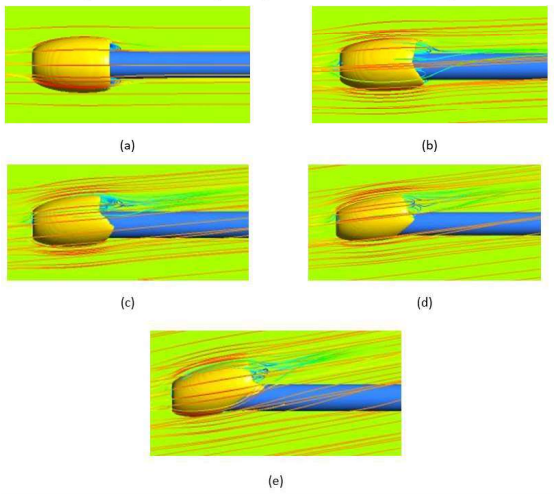

Fig 10: 3-d flow field about blunt fore-body at several angle of attack (a, b, c, d and e are 0, 2.5, 5, 7.5 and 10 angle of attack respectively), Cavitation number =0.29 and liquid volume fraction =0.8 isosurface.

CONCLUSIONS

In the current study, multi-block structured meshes were generated, for the different case studies and the numerical simulation was performed in a wide range of cavitation numbers. The conclusions apply for axisymmetric body:

- Comparison between experimental and achieved numerical simulation results for cavity geometry (length and cavity width) show good agreement.
- The variation of drag coefficient for infinity length of the cavity about disk cavitator is under 1 percent clearly demonstrating the accuracy of Reichardt's semi-empirical formula, which treats it as constant.
- The pressure distributions associated with natural cavitation are well predicted for a cylindrical body with a blunt fore-body.
- Weaknesses in the current work were observed in the cone fore-body analyses.

And, several interesting features are observed in the three-dimensional results as follow:

- The flows are seen to be highly three dimensional.
- A recirculation zone at the end of cavity is larger in the higher angle of attack.
- The bubble is shown to have its greatest axial extent off in the symmetry plane.

REFERENCES

[1] N.H.Singhal, A.K.Athavale, M.Li and Y.Jiang, Mathematical basis and validation of the full cavitation model, J.Fluids Eng., Vol. 124, 1-8, (2002).
[2] C.L.Merkle, J.Feng, and P.E.O.Buelow, Computational modeling of the dynamics of sheet cavitation, Proceeding of the 3rd International Symposium on Cavitation, (CAV98), Gernoble, France, (1998).
[3] R.F.Kunse, D.A.Boger, D.A.Stinberg, T.S.Chyczewski, J.W.Lindau, and H.J.Gibeling, A preconditioned Navier-Stokes method for two-phase flows with application to cavitation, Computers & Fluids, Vol. 29, 849-875, (2000).
[4] R.F.Kunse, D.A.Boger, D.A.Stinberg, T.S.Chyczewski, H.J.Gibeling, S.Vencateswaran, and T.A.Govindan, A preconditionated Navier-Stokes method for two-phase flows with application to cavitation prediction, Computers & Fluids, 29, 849-875 (2000).
[5] J.W.Lindau, R.F.Kunse, Advancement and application of multiphase CFD modeling to high speed supercavitating flows, Final report SF298 final report, (2004).
[6] J.Sauer and G.H.Schnerr, Unsteady cavitating flow – a new cavitation model based on modified front capturing method and bubble dynamics, In Proc. Of FEDSM00 4th Fluids Engineering Summer Conference, (2000).
[7] I.Senocak, and W.Shyy, A pressure-based method for turbulent cavitating flow computations, J, Comput. Phys, 176, 363–383, (2002).
[8] I.Senocak, Computational Methodology for the Simulation Turbulent Cavitating Flows. PhD thesis, University of Florida, (2002).
[9]CFX-ANSYS Canada Ltd. CFX-5.7: Solver Theory. Canada, (2004).
[10] H.K.Versteegand and W.Malalasekera, An introduction to Computational Fluid Dynamics: The finite volume method, vol. Pearson Prentice Hall, (1995).

[11] H.Rouse and J.S.McNwon, Cavitation and pressure distribution head form at zero of angle of yaw, Studies in engineering bulletin 32, state university of lowa, (1948).
[12] M.Self and J.F.Ripken, steady-state cavity studies in a free-jet water tunnel, St. Anthony Falls Hydr. Lab. rep. 47, (1955).
[13] Robert T. Knapp, James W. Daily, Frederick G. Hammit, Cavitation, McGraw Hill Inc, (1970).
[14] C.Brennen, A numerical solution of axisymmtric cavity flows, Fluid Mechanics, 37, 671-688, (1968).